Check for updates

Mechanochemical synthesis of Sb^{3+}-doped Cs$_2$ZrCl$_6$ double perovskites for excitation-wavelength-responsive trimodal luminescence and high-level anti-counterfeiting†

Qiaochu Chen,[a] Xuehan Ma,*[b] Guifu Dong [ID] [a] and Hongbin Yan [ID] *[a]

All-inorganic lead-free halide perovskites have shown great promise in the field of optoelectronics. However, the room-temperature, low-cost, and large-scale synthesis of such materials remains challenging. Here, we report a rapid mechanochemical synthesis strategy based on ethanol-assisted ball milling to successfully prepare Cs$_2$ZrCl$_6$ double perovskite with Sb^{3+} doping, which exhibits tricolor luminescence with excitation wavelength-dependent characteristics. The material emits blue (450 nm, [ZrCl$_6$]$^{2-}$ self-trapped exciton emission), warm white (450/610 nm dual peaks), and red (610 nm, Sb^{3+} ^{3}P$_1$ → ^{1}S$_0$ transition) light under 254, 310, and 365 nm ultraviolet excitation, respectively, with a photoluminescence quantum yield (PLQY) stably exceeding 30%. When the Cs$_2$ZrCl$_6$:Sb^{3+} samples are fabricated into anti-counterfeiting patterns, they emit blue, warm white, and red light under 254, 310, and 365 nm ultraviolet lamp excitation, respectively, demonstrating excellent application prospects in the field of anti-counterfeiting encryption. This study provides a new idea for the development of efficient and environmentally friendly synthesis of multi-modal anti-counterfeiting materials.

1 Introduction

Although lead-based perovskites have shown remarkable performance in areas such as solid-state lighting for illumination and display, as well as photodetectors, concerns about the toxicity of lead and their environmental instability have limited their large-scale application.[1,2] Therefore, lead-free metal halide perovskites and their derivatives with superior stability have become promising alternatives.[3] The zero-dimensional perovskites of the type Cs$_2$B^{IV}X$_6$ (where B^{IV} = Sn^{4+}, Zr^{4+}, Hf^{4+} and Te^{4+}) offer a range of advantages. Their unique isolated [B^{IV}X$_6$]$^{2-}$ octahedral structure effectively reduces non-radiative recombination by confining carriers strongly, leading to highly efficient luminescence.[4,5] The spatial isolation of host/guest excitons allows for the independent luminescence of host self-trapped excitons and doped excitons, which in turn enables dynamic spectral regulation.[6] The Sb^{3+} ions, which contain 5s^2 lone pair electrons, are capable of producing dual-band emissions of blue and orange light *via* self-trapped excitons (STEs).[7,8] Cs$_2$ZrCl$_6$, being a vacancy-ordered double perovskite, exhibits high thermal and chemical stability. Since the

coordination environment of Zr^{4+} is similar to that of Sb^{3+}, it makes an ideal host material for Sb^{3+} doping, allowing for the regulation of optical properties.[9]

Currently, the primary preparation methods for double perovskites involve liquid-phase approaches, including solvothermal synthesis, supersaturation crystallization, and hot injection techniques.[10,11] The liquid-phase methods inevitably require a substantial amount of organic solvents in the process of synthesis, separation and purification, which brings the problem of environmental pollution and limits its further development in the lighting and display industries.[12,13] The traditional high-temperature/high-pressure synthesis methods (such as hydrothermal method) have complex processes, low yield and are difficult to be scaled up.[14] Compared with the solution method, the ball milling method for synthesizing perovskites does not require hydrochloric acid or organic solvents, inert gas protection or high-temperature treatment, and can be operated at room temperature and in an open environment, with advantages such as batch preparation, and is expected to be promoted in the industrial application of perovskite optoelectronic devices.[15] Samanta *et al.* synthesized cesium lanthanide chlorides (Cs$_3$LnCl$_6$, Ln = Ce, Tb, Eu) on a large scale through mechanochemical methods and applied them in the field of radioluminescence, greatly simplifying the complex processes of traditional solid-state/solution methods.[2] Pi *et al.* synthesized Cs$_2$NaBiCl$_6$ porous microspheres through a simple grinding method for photocatalytic CO$_2$ reduction.[16]

[a]*Hunan Automotive Engineering Vocational University, Zhuzhou 412001, P. R. China. E-mail: yanhb_18238@163.com*

[b]*School of Packaging Design and Art, Hunan University of Technology, Zhuzhou 412007, P. R. China. E-mail: 19862103812@163.com*

† Electronic supplementary information (ESI) available. See DOI: https://doi.org/10.1039/d5ra03637b

Chen *et al.* achieved the universal synthesis of $APbX_3$ (A = MA, FA, Cs; X = Cl, Br, I) nanocrystals through a room-temperature grinding method and constructed UV-excited white LEDs.[17]

Inspired by the aforementioned studies, we employed ethanol solution as the carrier and successfully fabricated Sb^{3+}-doped Cs_2ZrCl_6 double perovskite trimodal luminescent materials for the first time *via* ball milling. The photoluminescence quantum yield (PLQY) of the prepared samples can be stably maintained at above 30%, while demonstrating remarkable tricolor emission under the excitation of 254, 310 and 365 nm. This facile and efficient solid-state strategy achieves multimode luminescence within a record-short processing time of 3 minutes, featuring scalable synthesis and potential for large-scale production. Comprehensive characterization through scanning electron microscopy (SEM), X-ray diffraction (XRD), and spectroscopic analysis systematically revealed the structural integrity and luminescence mechanisms. Detailed investigation confirms the coexistence of self-trapped exciton emission and Sb^{3+}-activated transitions, accounting for the unique wavelength-dependent chromaticity modulation. Our findings present a paradigm-shifting approach for developing environmentally benign optical security materials, offering significant advantages in rapid fabrication, multilevel encryption capability, and industrial scalability.

2 Results and discussion

Fig. 1a schematically depicts the mechanical ball milling synthesis process of Sb^{3+} doped Cs_2ZrCl_6 double perovskite under ambient conditions. The precursor mixture CsCl, $ZrCl_4$, and $SbCl_3$ underwent high-energy (HE) ball milling with zirconia grinding media in ethanol solvent. This process harnessed intense collisions, shear forces, and friction between grinding balls and reactants to convert mechanical energy into chemical activation, effectively disrupting precursor lattice structures.[13,18] The high-dielectric ethanol solvent facilitated ion dissociation *via* strong coordination effects, transforming the conventional solid–solid reaction into a quasi-solid–liquid interfacial process.[19–22] Mechanical impacts enhanced atomic/ionic diffusion efficiency through three critical mechanisms: (1) forced intimate contact between precursor particles enabled efficient mass transfer. (2) Localized temperature spikes at collision sites promoted bond reorganization and crystallization.[12,23] (3) Progressive particle size reduction (down to submicron scale) continuously exposed fresh reactive surfaces, driving the sequential assembly of $[ZrCl_6]^{2-}$ and $[SbCl_6]^{3-}$ octahedral frameworks.[10,24] Fig. S1† presents the photograph of the bright orange luminescence emitted by the large-scale synthesized Cs_2ZrCl_6:2.5% Sb^{3+} microcrystalline powder under 310 nm excitation, along with the physical image of gram-scale production. This highlights the material's capability for large-scale preparation and its promising performance in luminescent applications.

Fig. 1b presents the scanning electron microscopy (SEM) morphology of as-synthesized Cs_2ZrCl_6:Sb^{3+}, revealing irregular microstructures with particle sizes spanning 0.3–1.5 μm. This heterogeneity originates from non-uniform stress distribution during milling selective particle fragmentation/agglomeration cycles created size/shape polydispersity, while excessive collisions induced secondary agglomerates with rough surfaces.[2,15,25] Nevertheless, energy-dispersive X-ray spectroscopy (EDS) mapping confirms homogeneous spatial distribution of Cs, Zr, Cl, and Sb^{3+} species within the perovskite lattice, verifying successful isovalent substitution without phase segregation (Fig. 1d–h). Table S1† presents the inductively coupled plasma emission spectrometer (ICP-OES) Cs_2ZrCl_6:2.5% Sb^{3+}, with quantified atomic ratios of Zr : Sb ≈ 97.8 : 2.2. This experimental stoichiometry closely aligns with the theoretical composition, demonstrating successful Sb^{3+} substitution while preserving the host lattice integrity. The preserved elemental homogeneity underscores the efficacy of our solvent-assisted mechanochemical strategy in achieving atomic-level doping control.

The Sb^{3+}-doped Cs_2ZrCl_6 system crystallizes in a cubic vacancy-ordered double perovskite structure (space group: $Fm\bar{3}m$), featuring isolated $[ZrCl_6]^{2-}$ octahedral units.[26,27] Fig. 2 compares the X-ray diffraction (XRD) patterns of pristine Cs_2ZrCl_6 and Sb^{3+}-doped derivatives across varying doping concentrations. Successful partial substitution of $[ZrCl_6]^{2-}$ octahedra by $[SbCl_6]^{3-}$ species is evidenced by the maintained phase purity, with all diffraction peaks aligning precisely with the cubic Cs_2ZrCl_6 reference (PDF# 74-1001) and no detectable impurity phases. The preferential occupation of Zr^{4+} sites (ionic radius: 0.73 Å) by Sb^{3+} (0.92 Å) over Cs^+ (1.69 Å) arises from two critical factors: (1) closer ionic radius compatibility, minimizing lattice strain; (2) isovalent substitution feasibility, preserving charge balance.[3,28] Remarkably, the structural integrity remains intact across all doping levels, as reflected in the invariant XRD peak profiles. Comparison with the Cs_2ZrCl_6 matrix material revealed that XRD patterns remained essentially unchanged after Sb^{3+} doping at varying concentrations, indicating that Sb^{3+}
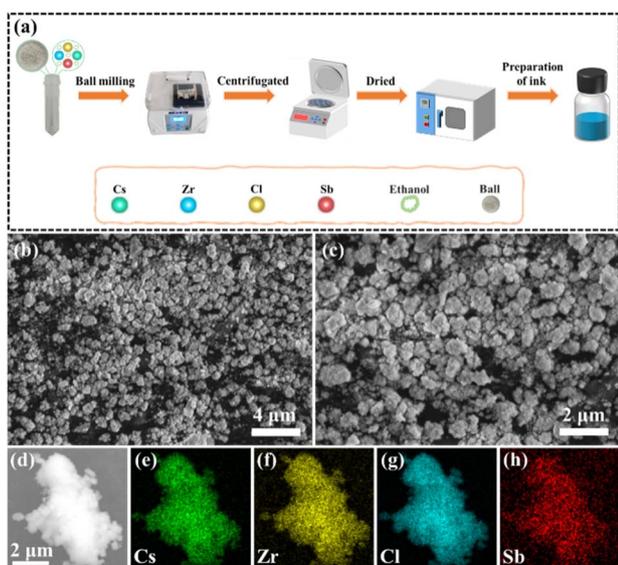

Fig. 1 (a) Schematic diagram of the preparation of Sb^{3+} doped Cs_2ZrCl_6 double perovskites. SEM images (b and c) and elemental mapping images (d–h) of Cs_2ZrCl_6:3% Sb^{3+}.

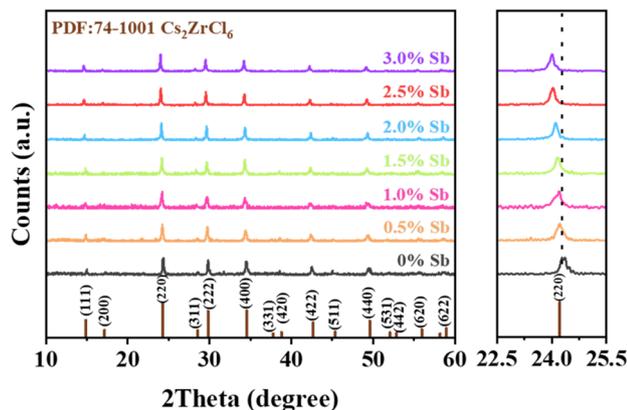Fig. 2   XRD patterns of Cs_2ZrCl_6 and Cs_2ZrCl_6:x% Sb^{3+} ($0 \leq x \leq 3\%$) samples.

Fig. 3   (a) Absorption spectra of Cs_2ZrCl_6:x Sb^{3+} (x = 0–3.5%). (b) PLE (monitored the emission at 450 nm) and (c) (monitored the emission at 610 nm) of Cs_2ZrCl_6:x% Sb^{3+} ($0 \leq x \leq 3\%$). PL spectra excited by (d) 254 nm, (e) 310 nm and (f) 365 nm of Sb^{3+}-doped DPs with various Sb^{3+} concentrations, respectively.

doping did not alter the host material's crystal structure. However, with increasing Sb^{3+} (0.90 Å) ion doping content, partial substitution of Zr^{4+} occurred, causing the (220) diffraction peak to gradually shift towards lower angles. This phenomenon suggests that Sb^{3+} incorporation induced lattice expansion in the sample.[9]

The non-bonding $5s^2$ lone pair electrons of Sb^{3+} retain high polarizability due to their chemically inert nature, enabling significant modulation of the ion's electronic configuration *via* strong coulombic repulsion.[28] In the ground state ($^1S_0$), these electrons adopt a spherically symmetric distribution, while photoexcitation promotes s → p orbital transitions, forming hybridized sp states (*e.g.*, $^1P_1$ or ^3P_J). This electronic restructuring induces pronounced Jahn–Teller distortions, splitting energy levels and lowering excited-state symmetry.[29] The enhanced electron–phonon coupling facilitates non-radiative relaxation from singlet to triplet states (^3P_J), ultimately enabling photon emission *via* the $^3P_1 \rightarrow {}^1S_0$ transition. This structural modification manifests as broadband emission with a large Stokes shift, characteristic of parity-forbidden transitions.[30] To maintain charge balance, the heterovalent substitution of $Sb^{3+} \rightarrow Zr^{4+}$ introduces a negative charge defect $[Sb_{Zr}]^-$, which needs to be compensated by a Cl vacancy $[V_{Cl}]^+$ to form a $[SbCl_5]^{2-}$ defect cluster, thereby affecting the luminescence properties.[31,32]

A systematic doping optimization framework was established through comprehensive spectroscopic investigations to determine the optimal Sb^{3+} incorporation ratio in Cs_2ZrCl_6. Fig. 3a presents the ultraviolet-visible (UV-Vis) absorption spectra of systematically doped samples. Undoped Cs_2ZrCl_6 exhibits weak absorption in the 250–350 nm range, confirming its intrinsically limited photon-harvesting capability. With increasing Sb^{3+} doping concentration, absorption intensity increases significantly, demonstrating that Sb^{3+} incorporation enhances light harvesting capability. The $5s^2$ electronic configuration of Sb^{3+} endows it with a unique lone-pair electron effect, facilitating self-trapped exciton formation and lattice coupling that strengthen optical absorption.[30] Absorption band broadening with minor redshifts at higher doping levels suggests
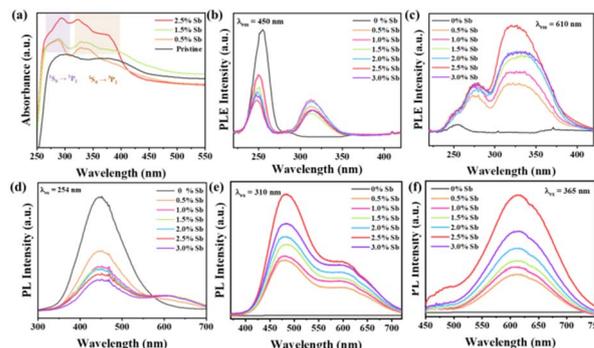
lattice distortion and band structure modification induced by aliovalent substitution. The absorption bands at 280–315 nm and 320–400 nm correspond to $^1S_0 \rightarrow {}^1P_1$ and $^1S_0 \rightarrow {}^3P_1$ transitions of Sb^{3+}, respectively.[29] The negligible absorption above 400 nm confirms UV-dominant optical responsiveness, positioning this material as a promising candidate for UV-selective photonic devices. Fig. 3b systematically elucidates the concentration-dependent excitation characteristics of Sb^{3+}-doped Cs_2ZrCl_6 (0–3.0% Sb^{3+}). Pure Cs_2ZrCl_6 only has an excitation peak near 250 nm, which is caused by the Zr–Cl charge transfer transition in the $[ZrCl_6]^{2-}$ octahedron. However, after doping with Sb^{3+}, new excitation peaks related to the electronic transitions of Sb^{3+} are introduced, expanding the material's light absorption range. The doping of Sb^{3+} ions suppresses the excitation of $[ZrCl_6]^{2-}$. As Sb^{3+} doping concentration increases, pronounced alterations in intensity and peak distribution of the excitation spectra are observed, with significant enhancement in certain wavelength ranges and the emergence of new excitation peaks within 280–360 nm. Progressive redshift of peak positions (for 0% Sb^{3+}) indicates electronic structure modification induced by Sb^{3+} doping.

The excitation profiles monitored at 610 nm reveal non-monotonic concentration dependence (Fig. 3c). At optimal doping (0.5–2.0%), enhanced excitation intensity and spectral resolution reflect improved radiative transitions through uniformly distributed luminescent centers. This regime maximizes photon harvesting *via* minimized non-radiative losses.[7] Conversely, further increasing doping to 3.0% triggers intensity saturation and linewidth broadening, signaling the onset of concentration quenching. At low concentrations, the luminescent centers exhibit uniform distribution, facilitating efficient energy absorption and radiative transitions. However, at high concentrations, the enhanced interaction between ions leads to concentration quenching, which inhibits further increases in excitation efficiency or may even cause a decline.[6,33]

Fig. 3d shows the emission spectrum of the sample under 254 nm ultraviolet excitation. When the excitation wavelength is fixed at 254 nm, the undoped Cs_2ZrCl_6 matrix material exhibits

blue emission with the emission center located around 450 nm and a half-peak width of approximately 115 nm, which is attributed to the STEs emission caused by the distortion of the $[ZrCl_6]^{2-}$ octahedron.[34,35] After introducing Sb^{3+} dopants into Cs_2ZrCl_6, a new orange emission band at 610 nm appears under 254 nm excitation. As the doping content of Sb^{3+} gradually increases, the blue emission of the Cs_2ZrCl_6 matrix continuously decreases while the peak position remains unchanged, indicating that the luminescence of the Cs_2ZrCl_6 host is not completely quenched. Besides, as presented in Fig. S2,† the normalized emission spectra under 254 nm UV excitation reveal a distinct enhancement in the intensity of the red emission peak centered at 610 nm with increasing Sb^{3+} doping concentration. As shown in Fig. 3e, under 310 nm excitation, Cs_2ZrCl_6:y% Sb^{3+} exhibits a dual-peak emission covering the range of 400–700 nm, with the maxima located at 490 nm and 610 nm respectively. This indicates that the doping of Sb^{3+} ions introduces additional luminescent centers.[36,37] As presented in Fig. S3,† analysis of normalized spectra shows no significant enhancement in the 610 nm emission peak intensity with increasing Sb^{3+} content, indicating that the dominant transition under 310 nm excitation corresponds to the $^1P_1 \rightarrow {}^1S_0$ electronic transition. Under the excitation of 310 nm light, electrons undergo a transition from the ground state to the excited state. After ultraviolet excitation, the significantly distorted $[SbCl_5]^{2-}$ promotes the rapid transition of electrons from the high-energy excited state to the low-energy (LE) excited state, and then the electrons transition to the ground state through singlet and triplet STEs respectively, generating low-energy and high-energy emissions, which causes a significant Stokes shift. The Stokes shifts of the high-energy emission (490 nm) and the low-energy (LE) emission (610 nm) are 180 nm and 300 nm respectively.[9,37] Under 310 nm excitation, the quantum efficiency of all Sb-ion-doped samples was found to exceed 30%, with the maximum value reaching 46.25% (Fig. S2†).

Based on existing research, it is speculated that the STEs emissions might be caused by the $[SbCl_5]^{2-}$ polyhedral dopant. Therefore, the high-energy band (490 nm) originates from the rapid radiative recombination of the singlet STEs ($^1P_1 \rightarrow {}^1S_0$), which is a spin-allowed dipole transition. While the low-energy band (610 nm) is dominated by the slow radiative transition of the triplet STEs ($^3P_1 \rightarrow {}^1S_0$), which is a spin-forbidden transition but partially allowed due to crystal field perturbation.[31] It can be seen from the PL spectrum that when the doping concentration of Sb^{3+} reaches 2.5%, the PL intensity reaches its maximum value. After that, due to excessive doping, the concentration quenching is caused by the increase of defects or energy transfer loss. Fig. 3f shows the emission spectra of Cs_2ZrCl_6 with different Sb^{3+} doping concentrations (0.5% to 3.5%) under 365 nm excitation. All samples show emission peaks in the range of 550 to 700 nm, and the spectral shapes are basically the same, indicating that the luminescence mechanism is consistent; however, the emission intensity varies with the doping concentration.

Generally speaking, the variation of the monitored excitation (emission) wavelength will lead to noticeable shifts and changes in the shape of the corresponding excitation (emission) peak.

The excitation and emission of the host and Sb^{3+} ions are independent of one another, allowing the relative intensity of high-energy and low-energy emissions to be adjusted by changing the excitation wavelength (Fig. 4 and S3†). As shown in Fig. 4a, when undoped, the fluorescence emission peaks are distributed over a wide ultraviolet region (240–320 nm), with weak intensity and broad peak shapes. This indicates that the undoped Cs_2ZrCl_6 host material itself has a relatively low luminescence efficiency, which may be attributed to the non-radiative recombination of the intrinsic $[ZrCl_6]^{2-}$ octahedron.[38] As shown in Fig. 4b, when doped at a low concentration (1.5% Sb^{3+}), the emission peak is significantly concentrated and the intensity is notably enhanced. The Sb^{3+} ions replace Zr^{4+} in the Cs_2ZrCl_6 lattice, promoting the transition of electrons from the excited state to the ground state and the release of photons, which significantly enhances the fluorescence intensity. As shown in Fig. 4c, when doped at a high concentration (2.5% Sb^{3+}), the density of luminescent centers increases, and the fluorescence intensity continues to rise.

Fig. 4d shows the PL decay curves of the double perovskite matrix materials doped with different contents of Sb^{3+} under ultraviolet excitation, with the emission wavelength of 610 nm monitored. As shown in the figure, under 365 nm excitation, the decay curves of all samples exhibit single-exponential or nearly single-exponential decay, indicating that the fluorescence decay is mainly dominated by a single mechanism. The average lifetime of the undoped Cs_2ZrCl_6 matrix material is 3.08 μs. With the incorporation of different contents of Sb^{3+}, the average lifetimes of the samples are 6.78 μs, 6.44 μs, and 6.61 μs (corresponding to 0.5%, 1.5%, and 2.5% Sb^{3+} doping concentrations, respectively).[37,39] The change in lifetime indicates that the incorporation of Sb^{3+} alters the luminescence source of the material. As the concentration of Sb^{3+} increases, the probability of energy transfer between ions increases, forming a more efficient energy transfer network and reducing the chance of the excited state being captured by non-radiative centers. Energy may be more likely to migrate between Sb^{3+} ions and eventually
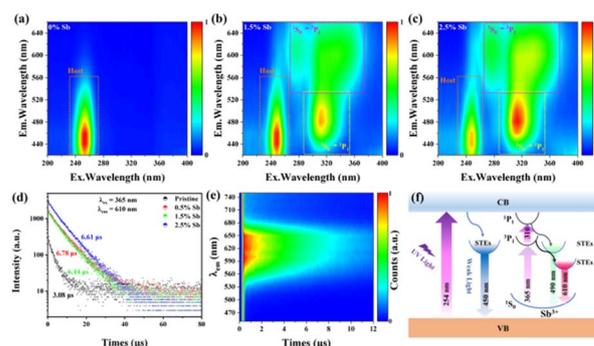

Fig. 4 Contour plots of the excitation-wavelength-dependent spectra of (a) Cs_2ZrCl_6, (b) Cs_2ZrCl_6:1.5% Sb^{3+} and (c) Cs_2ZrCl_6:2.5% Sb^{3+} under different emission wavelengths. (d) PL decay curves obtained for Cs_2ZrCl_6:x% Sb^{3+} (x = 0, 0.5, 1.5, 2.5) MCs against the excitation wavelengths of 365 nm and by monitoring the emission at 610 nm. (e) TRPL spectra of Cs_2ZrCl_6:2.5% Sb^{3+} within a time window of 10 μs. (f) Diagram of photophysical process of Cs_2ZrCl_6:Sb^{3+}.

be released through radiative recombination rather than being quenched by defects.[5]

When the Sb^{3+} concentration exceeds the critical value (such as 2.5%), the distance between adjacent luminescent centers decreases, and the excited state energy is dissipated through cross-relaxation or energy transfer to quenching sites (such as surface defects, grain boundaries), significantly reducing the lifetime. To observe the radiative transition of the Sb^{3+} excited-state electron from the excited state ($5s^1\ 5p^1$) to the ground state ($5s^2$), time-resolved photoluminescence (TRPL) spectra were collected for the doped crystals. Similar to the steady-state measurements, the TRPL spectra contain peaks located at 520–700 nm. Specifically, the emission of Sb^{3+} from $^3P_1 \to {}^1S_0$ can be clearly observed within a short time window, as shown in Fig. 4e. Fig. 4f illustrates the photophysical processes and luminescence mechanism of Cs_2ZrCl_6:Sb^{3+} material. The $5s^2$ lone pair electrons of Sb^{3+} form a strong electron–phonon coupling in the lattice, leading to the self-trapping of singlet ($^1P_1 \to {}^1S_0$) and triplet ($^3P_1 \to {}^1S_0$) excitons, which emit blue and orange light, respectively. Electrons are excited from the ground state ($^1S_0$) to the excited state and recombine through STEs of the host material $[ZrCl_6]^{2-}$, generating blue light emission (450 nm). When excited at 310 nm, electrons enter high-energy states through $^1S_0 \to {}^1P_1$ (singlet) and $^1S_0 \to {}^3P_1$ (triplet) transitions, accompanied by energy transfer from $^1P_1$ to $^3P_1$. Electrons are captured by singlet STEs (STEs 1) and triplet STEs (STEs 2), and finally recombine to emit blue (490 nm) and orange (610 nm) light. When excited at 360 nm, only the $^1S_0 \to {}^3P_1$ transition is excited, generating orange light (610 nm). Therefore, the relative intensities of STEs 1 and STEs 2 can be controlled by adjusting the doping concentration of Sb^{3+} or the excitation wavelength. As presented in Fig. S4,† after being stored in ambient air (humidity: 35–70%, temperature: 15–33 °C) for 10 days and continuously irradiated with ultraviolet light (λ_{ex} = 365 nm, 12.3 mW cm^{-2}) for 10 days, the Cs_2ZrCl_6:2.5% Sb^{3+} retained a high luminescence efficiency. This demonstrates the material's excellent stability under such conditions.

The Cs_2ZrCl_6:0.5% Sb^{3+} sample demonstrates remarkable application potential in advanced optical anti-counterfeiting. Selective excitation at 254 nm or 310 nm enables distinct activation of either host-derived STEs emission or Sb^{3+}-doped STEs emission, respectively, achieving dynamic color modulation. Through screen-printing technology, we fabricated anti-counterfeiting patterns on weighing paper and commercial packaging substrates (Fig. 5a). As shown in Fig. 5b and c, the latent patterns remain invisible under ambient light but reveal watermarks upon UV illumination. The material exhibits wavelength-responsive optical characteristics, displaying programmable chromic transitions under specific UV excitations (254 nm, 310 nm, and 365 nm). Each excitation–emission pair constitutes an independent encryption/decryption channel, establishing triple-level cryptographic conversion within a single-component system.[40,41] This excitation-dependent multimodal anti-counterfeiting mechanism significantly enhances security through optical complexity. Practical implementation on KN95 mask packaging demonstrates that customized optical signatures can be exclusively revealed under
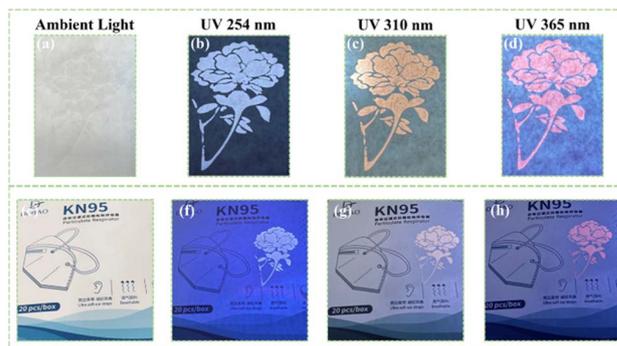

Fig. 5 Cs_2ZrCl_6:0.5% Sb^{3+} sample preparation of screen printing anti-counterfeiting pattern under the room light (a) and the pattern excited under the (b) 254 nm, (c) 310 nm, (d) 365 nm. (e–h) Display of the anti-counterfeiting function on the package.

predetermined UV irradiation conditions. Fig. 5e–h systematically presents the prototype demonstration with excitation conditions corresponding to Fig. 5a–d. The developed material enables covert yet distinguishable authentication markers, providing enhanced tamper resistance and security for commercial products. This strategy creates an information encryption hierarchy through photon-programmable luminescence switching, representing a significant advancement in high-security optical anti-counterfeiting technologies.

3   Conclusions

This study demonstrates a breakthrough in rapid material synthesis through an ethanol-assisted mechanochemical approach, achieving controlled preparation of Sb^{3+}-doped Cs_2ZrCl_6 double perovskite within 3 minutes. This innovative strategy overcomes the limitations of conventional hydrothermal methods, including time-consuming processes and reliance on toxic solvents. The aliovalent substitution of Zr^{4+} by Sb^{3+} induces lattice distortion, creating dual emission centers ($[ZrCl_6]^{2-}$/$[SbCl_6]^{3-}$) that enable wavelength-selective luminescence. Remarkably, triple emission modes are activated under distinct UV excitations (254/310/365 nm), circumventing the phase-segregation challenges inherent in multi-component systems. A novel PEG/ethanol-based fluorescent ink system was developed to implement "ambient-light-invisible/UV-responsive" trimodal anti-counterfeiting patterns on commercial packaging substrates. The printed designs exhibit complete transparency under natural illumination while revealing encrypted chromatic information under specific UV wavelengths. This work establishes a pioneering paradigm for designing optical anti-counterfeiting materials that synergize rapid fabrication, environmental compatibility, and high-security encryption. The demonstrated photon-decoding mechanism and scalable screen-printing compatibility provide transformative opportunities for next-generation information security technologies.

4 Experimental

4.1 Materials

Cesium chloride (CsCl, Aladdin, 99.99%), zirconium(IV) chloride (ZrCl$_4$, Aladdin, 98%), chlorid antimonity (SbCl$_3$, Aladdin, 99.9%), ethanol (Aladdin, 95%) and zirconia grinding balls (55–65% ZrO$_2$, 35–45% SiO$_2$, 4.1 g cm^{-3}, 0.5 mm, Aladdin). All materials were used without further purification.

4.2 Preparation of Sb^{3+} doped Cs$_2$ZrCl$_6$ phosphor

An appropriate amount of SbCl$_3$ is dissolved in an appropriate amount of ethanol to prepare a mixed solution. Then, according to the required doping ratio, CsCl (2 mmol), ZrCl$_4$ (1 mmol), ethanol (1000–x μL) and SbCl$_3$ mixed solution (x μL) are placed in 2-mL ball mill tank (after the ball mill tank is expanded, the reagent can be increased according to the corresponding proportion). Add 15 zirconia (ZrO$_2$) balls with a diameter of 0.5 mm into the ball mill tank. At a vibration speed of 500 (the maximum vibration speed of the machine), the ball mill reaction can be made in 3 minutes. The resulting sample was centrifuged and washed with ethanol for more than three times. Then dry in a drying oven at 60 °C for 10 minutes. The dried powder is screened with the ball mill for further characterization and application.

Attention: SbCl$_3$ samples are highly hygroscopic, and upon exposure to moisture, a hydrolysis reaction occurs, leading to the formation of antimony oxychloride (SbOCl) and hydrochloric acid (HCl).

$$SbCl_3 + H_2O \rightarrow SbOCl\downarrow + 2HCl$$
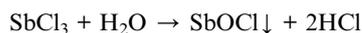
Therefore, it is recommended to store SbCl$_3$ samples in a sealed or vacuum environment whenever possible to minimize exposure to moisture. Hydrolysis of SbCl$_3$ can lead to the formation of byproducts that adversely affect luminescent efficiency.

4.3 Preparation of Sb^{3+} doped Cs$_2$ZrCl$_6$ anti-counterfeiting pattern

4.0 g of polyethylene glycol (PEG) and 10 mL of ethanol were combined and heated at 90 °C for 1 minute to dissolve the PEG/ethanol solution. Subsequently, 300 mg of the prepared Cs$_2$ZrCl$_6$:x% Sb^{3+} phosphor was added to each 1 mL of the solution. The mixture was subjected to ultrasonication for 10 minutes, followed by vigorous magnetic stirring at room temperature for 40 minutes. Once the solution is prepared, the screen printing screen can be utilized for printing.

4.4 Characterization

The structure and morphology of the DPs MCs were characterized by field emission scanning electron microscopy (SEM, S-4800, Hitachi, Japan), X-ray diffraction (XRD, D8 Advance, Bruker, Germany), and transmission electron microscopy (TEM, JEM-2100F, JEOL, Japan). The element distributions of the as-prepared samples were determined by energy-dispersive X-ray spectroscopy (EDX, Quantax-STEM, Bruker, Germany). The steady-state PL spectra, PL QYs, and PL decay curves were recorded using a spectrometer (Fluromax-4P, Horiba Jobin Yvon, Paris, France) equipped with a QY accessory and a time-correlated single-photon-counting (TCSPC) spectrometer.

Data availability

The data that support the findings of this study are available on request from the corresponding author, upon reasonable request.

Conflicts of interest

The authors declare that they have no known competing financial interests or personal relationships that could have appeared to influence the work reported in this paper.

Acknowledgements

Notes and references

1 F. Li, L. Cao, S. Shi, H. Gao, L. Song, C. Geng, W. Bi and S. Xu, *Angew. Chem., Int. Ed.*, 2019, **58**, 17631–17635.
2 T. Samanta, J. H. Han, H. U. Lee, B. K. Cha, Y. M. Park, N. S. M. Viswanath, H. B. Cho, H. W. Kim, S. B. Cho and W. B. Im, *Inorg. Chem.*, 2024, **63**, 16483–16490.
3 J. Jiang, Z. Du, H. Fu, W. Li, H. Zhang, H. Xie, J. Zheng and W. Yang, *Adv. Opt. Mater.*, 2024, **12**, 2401347.
4 H. Li, Y. Zhang, M. Zhou, H. Ding, L. Zhao, T. Jiang, H. Y. Yang, F. Zhao, W. Chen and Z. Teng, *ACS Energy Lett.*, 2022, **7**, 2876–2883.
5 I. Infante and L. Manna, *Nano Lett.*, 2020, **21**, 6–9.
6 Z. Liu, X. Ji, Z. Ma, F. Zhang, X. Qi, X. Chen, D. Wu, Y. Liu, M. Jia and X. Li, *Laser Photonics Rev.*, 2023, **17**, 2300094.
7 H. Arfin, A. S. Kshirsagar, J. Kaur, B. Mondal, Z. Xia, S. Chakraborty and A. Nag, *Chem. Mater.*, 2020, **32**, 10255–10267.
8 D. Zhu, M. L. Zaffalon, J. Zito, F. Cova, F. Meinardi, L. De Trizio, I. Infante, S. Brovelli and L. Manna, *ACS Energy Lett.*, 2021, **6**, 2283–2292.
9 F. Zhang, X. Chen, X. Qi, W. Liang, M. Wang, Z. Ma, X. Ji, D. Yang, M. Jia and D. Wu, *Nano Lett.*, 2022, **22**, 5046–5054.
10 J. Xu, G. Chen, T. Yang, H. Wu, L. Li, C. Ma, C. Zhu, Y. Wu, B. Liu and A. Hu, *J. Lumin.*, 2023, **255**, 119606.
11 C. Wang, H. Wang, M. Sun and G. Zhao, *CCS Chem.*, 2023, **5**, 1982–1988.
12 C. Zhao, Y. Gao, J. Wang and J. Qiu, *Laser Photonics Rev.*, 2024, **18**, 2300952.

13 G. García-Espejo, D. Rodríguez-Padrón, R. Luque, L. Camacho and G. de Miguel, *Nanoscale*, 2019, **11**, 16650–16657.

14 J. Jiang, J. Zheng, H. Fu, H. Zhang, D. Ou, Q. Chen, K. Wang, S. Cao, J. Zhao and Z. Du, *Chem. Eng. J.*, 2024, **479**, 147543.

15 J. Kim, N. T. Manh, H. T. Thai, S.-K. Jeong, Y.-W. Lee, Y. Cho, W. Ahn, Y. Choi and N. Cho, *Nanomaterials*, 2022, **12**, 920.

16 J. Pi, X. Jia, Z. Long, S. Yang, H. Wu, D. Zhou, Q. Wang, H. Zheng, Y. Yang and J. Zhang, *Adv. Energy Mater.*, 2022, **12**, 2202074.

17 D. Chen, J. Li, X. Chen, J. Chen and J. Zhong, *ACS Appl. Mater. Interfaces*, 2019, **11**, 10059–10067.

18 L. Cao, S. Shi, F. Li, Z. Tian, S. Xu and C. Geng, *Chem. Eng. J.*, 2022, **434**, 134693.

19 W. Fan, K. Deng, Y. Shen, Y. Bai and L. Li, *Angew. Chem., Int. Ed.*, 2022, **61**, e202211259.

20 S. Zuo, W. Niu, S. Chu, P. An, H. Huang, L. Zheng, L. Zhao and J. Zhang, *J. Phys. Chem. Lett.*, 2023, **14**, 4876–4885.

21 J. C. Hamill Jr, J. Schwartz and Y.-L. Loo, *ACS Energy Lett.*, 2017, **3**, 92–97.

22 S. Cheng and H. Zhong, *J. Phys. Chem. Lett.*, 2022, **13**, 2281–2290.

23 P. Xia, S. Zhang, J. Qu, X. Li, C. Lu, S. Xu and C. Wang, *Chem. Eng. J.*, 2023, **470**, 144319.

24 H. Xiao, H. Xiong, P. Li, L. Jiang, A. Yang, L. Lin, Z. Kang, Q. Yan and Y. Qiu, *Chem. Commun.*, 2022, **58**, 3827–3830.

25 K. Zhang, W. Fan, T. Yao, S. Wang, Z. Yang, J. Yao, L. Xu and J. Song, *Adv. Mater.*, 2024, **36**, 2310521.

26 J. Sun, W. Zheng, P. Huang, M. Zhang, W. Zhang, Z. Deng, S. Yu, M. Jin and X. Chen, *Angew. Chem., Int. Ed.*, 2022, **134**, e202201993.

27 F. Zhang, Y. Zhou, Z. Chen, M. Wang, Z. Ma, X. Chen, M. Jia, D. Wu, J. Xiao and X. Li, *Adv. Mater.*, 2022, **34**, 2204801.

28 Y. Jing, Y. Liu, J. Zhao and Z. Xia, *J. Phys. Chem. Lett.*, 2019, **10**, 7439–7444.

29 R. Hao, M. Liu, M. Yin and C.-K. Duan, *J. Phys. Chem. C*, 2023, **127**, 3742–3749.

30 F. Jiang, Z. Wu, M. Lu, Y. Gao, X. Li, X. Bai, Y. Ji and Y. Zhang, *Adv. Mater.*, 2023, **35**, 2211088.

31 Z. Huang, J. Zheng, H. Fu, J. Jiang, Z. Li, C. Gu, Z. Du, Y. Yang, W. Yang and J. Zhao, *J. Mater. Chem. C*, 2024, **12**, 2053–2062.

32 S. D. Adhikari, C. Echeverría-Arrondo, R. S. Sánchez, V. S. Chirvony, J. P. Martínez-Pastor, S. Agouram, V. Muñoz-Sanjosé and I. Mora-Seró, *Nanoscale*, 2022, **14**, 1468–1479.

33 S. Gong, R. Wu, S. Yang, L. Wu, M. Zhang, Q. Han and W. Wu, *Photonics Res.*, 2021, **9**, 2182–2189.

34 F. Zhang, W. Gao, G. J. Cruz, Y.-y. Sun, P. Zhang and J. Zhao, *Phys. Rev. B*, 2023, **107**, 235119.

35 S. Liu, B. Yang, J. Chen, D. Zheng, Z. Tang, W. Deng and K. Han, *Laser Photonics Rev.*, 2022, **16**, 2100439.

36 G. Xiong, L. Yuan, Y. Jin, H. Wu, B. Qu, Z. Li, G. Ju, L. Chen, S. Yang and Y. Hu, *J. Mater. Chem. C*, 2021, **9**, 13474–13483.

37 H. Arfin and A. Nag, *J. Phys. Chem. Lett.*, 2021, **12**, 10002–10008.

38 B. Chen, Y. Guo, Y. Wang, Z. Liu, Q. Wei, S. Wang, A. L. Rogach, G. Xing, P. Shi and F. Wang, *J. Am. Chem. Soc.*, 2021, **143**, 17599–17606.

39 X. Li, S. Xu, F. Liu, J. Qu, H. Shao, Z. Wang, Y. Cui, D. Ban and C. Wang, *ACS Appl. Mater. Interfaces*, 2021, **13**, 31031–31037.

40 M. Chen, X. Zhang, C. Luo, R. Qi, H. Peng and H. Lin, *ACS Appl. Mater. Interfaces*, 2021, **13**, 20622–20632.

41 R. Liu, W. Zhang, G. Li and W. Liu, *Inorg. Chem. Front.*, 2021, **8**, 4035–4043.